

# Laser-free GHz stroboscopic transmission electron microscope: Components, system integration, and practical considerations for pump–probe measurements F

Cite as: Rev. Sci. Instrum. **91**, 021301 (2020); <https://doi.org/10.1063/1.5131758>

Submitted: 15 October 2019 . Accepted: 01 February 2020 . Published Online: 24 February 2020

June W. Lau , Karl B. Schliep, Michael B. Katz, Vikrant J. Gokhale , Jason J. Gorman, Chunguang Jing, Ao Liu, Yubin Zhao, Eric Montgomery, Hyeokmin Choe, Wade Rush, Alexei Kanareykin, Xuewen Fu, and Yimei Zhu

## COLLECTIONS

F This paper was selected as Featured



View Online



Export Citation



CrossMark

## ARTICLES YOU MAY BE INTERESTED IN

[Photonic integration for UV to IR applications](#)

APL Photonics **5**, 020903 (2020); <https://doi.org/10.1063/1.5131683>

[Laser-less TEM provides time-resolved images of cyclical phenomena](#)

Scilight **2020**, 091101 (2020); <https://doi.org/10.1063/10.0000842>

[Performance of a ferroelectric glass electrolyte in a self-charging electrochemical cell with negative capacitance and resistance](#)

Applied Physics Reviews **7**, 011406 (2020); <https://doi.org/10.1063/1.5132841>

Lock-in Amplifiers

Find out more today



 Zurich Instruments



# Laser-free GHz stroboscopic transmission electron microscope: Components, system integration, and practical considerations for pump–probe measurements



Cite as: *Rev. Sci. Instrum.* **91**, 021301 (2020); doi: [10.1063/1.5131758](https://doi.org/10.1063/1.5131758)

Submitted: 15 October 2019 • Accepted: 1 February 2020 •

Published Online: 24 February 2020



View Online



Export Citation



CrossMark

June W. Lau,<sup>1,a)</sup>  Karl B. Schliep,<sup>1</sup> Michael B. Katz,<sup>1</sup> Vikrant J. Gokhale,<sup>2</sup>  Jason J. Gorman,<sup>2</sup> Chunguang Jing,<sup>3,b)</sup> Ao Liu,<sup>3</sup> Yubin Zhao,<sup>3</sup> Eric Montgomery,<sup>3</sup> Hyeokmin Choe,<sup>3</sup> Wade Rush,<sup>3</sup> Alexei Kanareykin,<sup>3</sup> Xuewen Fu,<sup>4</sup> and Yimei Zhu<sup>4,c)</sup>

## AFFILIATIONS

<sup>1</sup>Materials Science and Engineering Division, National Institute of Standards and Technology, Gaithersburg, Maryland 20899, USA

<sup>2</sup>Microsystems and Nanotechnology Division, National Institute of Standards and Technology, Gaithersburg, Maryland 20899, USA

<sup>3</sup>Euclid Techlabs, LLC, 365 Remington Blvd., Bolingbrook, Illinois 60440, USA

<sup>4</sup>Department of Condensed Matter Physics and Materials Science, Brookhaven National Laboratory, Upton, New York 11973, USA

<sup>a)</sup>Author to whom correspondence should be addressed: [june.lau@nist.gov](mailto:june.lau@nist.gov)

<sup>b)</sup>Electronic mail: [c.jing@euclidtechlabs.com](mailto:c.jing@euclidtechlabs.com)

<sup>c)</sup>Electronic mail: [zhu@bnl.gov](mailto:zhu@bnl.gov)

## ABSTRACT

A 300 keV transmission electron microscope was modified to produce broadband pulsed beams that can be, in principle, between 40 MHz and 12 GHz, corresponding to temporal resolution in the nanosecond to picosecond range without an excitation laser. The key enabling technology is a pair of phase-matched modulating and de-modulating traveling wave metallic comb striplines (pulsers). An initial temporal resolution of 30 ps was achieved with a strobe frequency of 6.0 GHz. The placement of the pulsers, mounted immediately below the gun, allows for preservation of all optical configurations, otherwise available to the unmodified instrument, and therefore makes such a post-modified instrument for dual-use, i.e., both pulsed-beam mode (i.e., stroboscopic time-resolved) and conventional continuous waveform mode. In this article, we describe the elements inserted into the beam path, challenges encountered during integration with an in-service microscope, and early results from an electric-field-driven pump–probe experiment. We conclude with ideas for making this class of instruments broadly applicable for examining cyclical and repeatable phenomena.

<https://doi.org/10.1063/1.5131758>

## I. INTRODUCTION

Transmission electron microscopy (TEM), and the associated analytical techniques, has long been considered a core-capability for materials and biological sciences due to its unparalleled ability in resolving spatial attributes such as morphology, structure, and chemistry. Up until about 15 years ago, the suite of electron

microscopy (EM) techniques was largely regarded as steady-state methods because few options for producing timed structures in an electron beam existed. Time-resolved EM was limited to a few hertz, determined by the readout rates of CCD cameras. Dynamic events faster than this would appear as motion blurring images, like those acquired by using a pinhole camera. A common example of motion-blurred in TEM images comes from thermally activated

ferromagnetic domain walls pinned between two or more potentials. These domain walls are blurred between anchoring defects, and frustratingly little can be learned about the magnitude of the pinning potentials.

Recently, important technological advancements have broadened the range of temporal resolution in the TEM. Commercial direct-counting and single-electron detectors can reveal dynamics in the ms-timescale.<sup>1–4</sup> Laser-actuated photoemission<sup>5–9</sup> and field-emission<sup>9</sup> microscopes combined with beam scanning, spatially parsed large area detectors,<sup>10</sup> and sparse-sensing algorithms<sup>11–13</sup> have impressively expanded the temporal range from  $\mu\text{s}$  to sub-ps timescales. Further optimization of the photoemission process could potentially extend temporal resolution deep into the fs-regime. Some photoemission processes produce single-shot, high-intensity pulses of electrons on demand ( $10^5$  electrons per shot), while others produce one electron per recharge cycle of the laser, rendering this type more suitable for stroboscopic operation. The benefits and limitations of single-shot vs stroboscopic modalities are succinctly summarized by Plemmons and Flannigan.<sup>14</sup> A pulsed electron beam was first demonstrated on a scanning electron microscope (SEM)<sup>15</sup> and, later, a TEM,<sup>16</sup> by engaging an electrostatic beam deflector in the kHz to MHz range. However, until recently, laser-triggered photoemission was the primary way to achieve faster, timed electron pulses in an electron microscope. In the last few years, periodic electron pulses have been demonstrated using a microwave cavity with a fixed resonant frequency in an SEM<sup>17</sup> and a TEM.<sup>18,19</sup>

The instrument in this article is a modified 300 keV  $\text{LaB}_6$  TEM (JEOL JEM3010).<sup>20</sup> This is the second successful modification of an in-service microscope; the first took place on a 200 keV Schottky emission TEM (JEM 2010F) at the JEOL USA headquarter in Peabody, MA. As there were substantial differences between the installations and in the experimental scope, the initial findings from the first installation were reported elsewhere.<sup>21</sup>

Periodic electron pulses on this instrument, as with the other, are continuously tunable between 40 MHz and 12 GHz. The primary purpose for this instrument is to examine cyclical and repeatable events in the stroboscopic mode. There are two ways to conduct a stroboscopic experiment: either (1) produce a pulsed beam with a frequency that matches exactly to a naturally occurring excitation frequency in the sample of interest, usually determined beforehand by an external measurement method, or (2) stimulate the sample at the same frequency (or integer harmonic) as the probe frequency, i.e., pump-probe. Other uses of a periodic electron beam for dose-rate management in beam-sensitive samples are also presently being investigated.

## II. DESIGN AND WORKING PRINCIPLES

The inspiration for the design and the construction of this GHz beam pulser originated from our desire to correlate dynamic events with physical properties in the microwave regime for several important material classes: ferromagnetics, ferroelectrics, spintronics, and magnonics. However, for such an instrument to be broadly applicable beyond niche applications, both the probe (periodic electron pulses) and the pump (sample excitation) signals must be broadband tunable with low jitter so that a broad range of materials with dynamics at different timescales can be accessed. The beam pulser was designed to preserve all native operation modes of the

unmodified instrument in the pulsed-beam mode, thus all modifications to this instrument were placed directly below the electron gun but before the microscope's original condenser lenses. Finally, when the pulsed beam is not in use (i.e., CW mode), the modified microscope should behave as the original unmodified instrument. Figure 1(a) shows a photograph of the post-modified microscope.

The two elements inserted into this microscope were (1) a pre-condenser lens, C0, and (2) the Euclid Strobe-300 pulser.<sup>20</sup> For a thermionic electron gun, the first crossover produced by the Wehnelt is generally located within the gun section. This leaves the operator with limited control over the spread of the emitted electrons entering down-column apertures. Therefore, the C0's function is to improve electron coupling and to provide the flexibility of placing the first beam crossover at an arbitrary point within the pulser. The C0 lens is a repurposed third-intermediate-projector compound lens from the JEOL 2000FX microscope.<sup>20</sup> The lens assembly is 127.3 mm tall and consists of a two-coil lens (C0A on the top and C0B on the bottom) and a flux-concentration pole piece. It has an inner beam tube (diameter = 3.15 mm) that functions as the vacuum liner. Next, we defined the optimum operation setting of C0 to coincide with the highest beam current achievable with the least

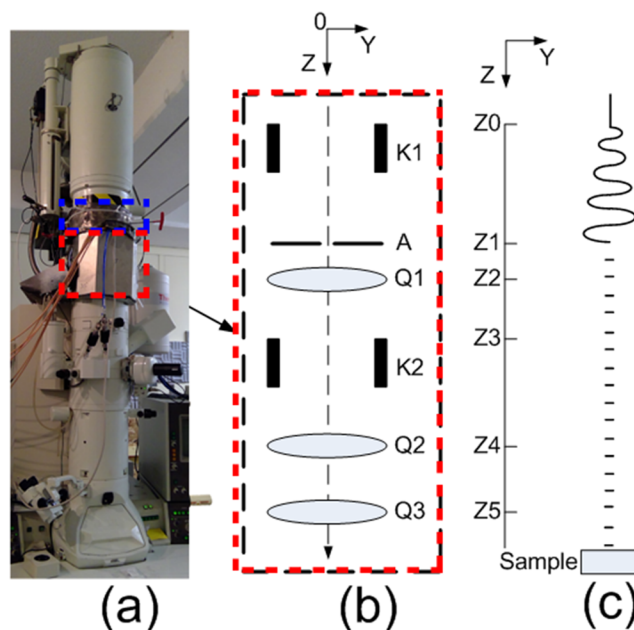


**FIG. 1.** (a) NIST's JEOL JEM-3010 TEM with the C0 (blue dotted rectangle) and the Euclid Strobe-300 pulser (red dotted rectangle) inserted between the gun and the standard column lens. (b) Schematic of the pulser's active elements and their relative locations. K1 and K2 are the beam modulator and de-modulator, respectively. The BCA is the beam-chopping aperture, and Q1, Q2, and Q3 are quadrupole steering magnets. Locations marked  $Z_0$ – $Z_5$  refer to the position of the active components relative to the exit face of the C0 lens, which is also the top of the pulser housing.  $Z_0 = 45$  mm,  $Z_1 = 95$  mm,  $Z_2 = 100$  mm,  $Z_3 = 155$  mm,  $Z_4 = 180$  mm, and  $Z_5 = 220$  mm. Schematic of the C0 is not shown. (c) Schematic of the electron beam in the pulsed-beam mode.

beam distortion. To do so, we operated both C0A and C0B independently from 0 mA to 620 mA, at 20 mA increments, and measured the beam current on the phosphor screen. In this case, the lenses which remained on are the following: condensers 1–3, condenser mini, and the projector. We found that the best beam quality was achieved with C0A at 340 mA and C0B off. To compute the focal length and to understand what this distance is relative to the pulser components, we had conducted a separate experiment using the same lens but on a stand-alone 200 keV electron gun (i.e., no lenses down-stream of the C0). In this experiment, the lens excitation was changed from 0 mA to 500 mA and the diameter of the beam was recorded on a YAG screen at three different distances. From this set of measurements, we determined that the focal length of C0A was 78 mm at 340 mA, as measured from the exit face of the compound lens. Since the focal length scales linearly with beam energy, the corresponding focal length for 300 keV electrons is 117 mm. Under this condition, the beam going into the pulser is convergent, with the crossover located approximately 5 mm down-stream of the beam chopping aperture (BCA), near the exit face of Q1 [see Fig. 1(b)]. This finding is consistent with the beam current measured at the phosphor screen using the BCA of different sizes, while the pulser was off. With all apertures downstream of the BCA fully retracted, Fig. 2 shows that the beam current is independent of BCA diameters accessible to us. Since the C0 crossover is so close to the BCA, the BCA allows all electrons to pass through in CW mode as long as it is centered. Water cooling of the C0 was provided by tapping into the serial water cooling line for the down-column lenses.

The pulser assembly is 242.6 mm tall, and Fig. 1(b) shows the active components within. The core innovation that produces the high repetition-rate broadband pulsed beams is a pair of Traveling Wave Metallic Comb Striplines (TWMCS). The TWMCS (marked K1 and K2) are traveling wave devices, each consisting of two metallic combs with “teeth” facing each other, as shown schematically in Fig. 3.

Features of the “teeth” such as the pitch ( $P$ ), width ( $t$ ), gap ( $d$ ), height ( $h$ ), and offset ( $b$ ) control and determine the phase velocity of

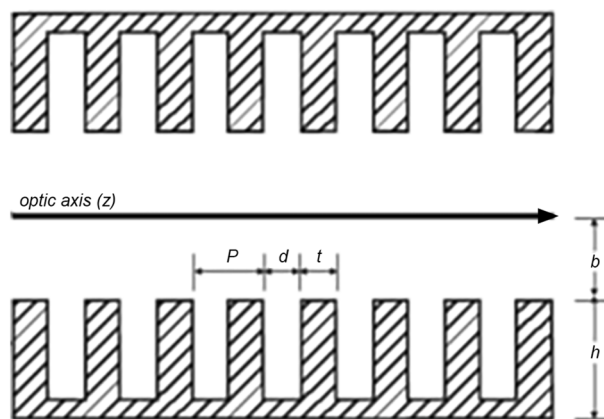


FIG. 3. Side view of the TWMCS.

the RF waves propagating through K1 and K2 in the transverse electromagnetic mode, whereby the phase velocity is substantially independent of the driving RF frequency over a wide frequency range. The dispersion relation is governed by the following equation:<sup>22</sup>

$$\frac{d}{P} \sum_{n=-\infty}^{\infty} \left[ \frac{1}{\tau_n h \tan(\tau_n b)} \left( \text{sinc} \frac{\beta_n d}{2} \right)^2 \right] = \frac{1}{kh \tan(kh)}, \quad (1)$$

where  $k$  is the wavenumber of the input RF,  $\tau_n$  and  $\beta_n$  are the order of propagation constants in the  $x$  (lateral) and  $z$  (longitudinal) direction, respectively. Equation (1) can be used to numerically calculate a family of dispersion relationship curves, and thus appropriate values of  $d$ ,  $t$ ,  $b$ , and  $h$  can be selected so as to match the phase velocity of the RF with the kinetic energy of the electrons.

The TWMCS are driven by a differential RF signal at one end of the comb and terminated at the other end with a 50  $\Omega$  load. In Fig. 4, we calculated the transmitted RF power through K1 and K2. It showed that RF can be efficiently coupled into the TWMCS up to

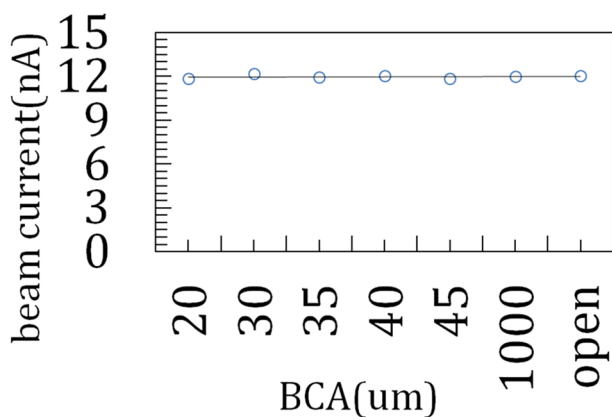


FIG. 2. The measured beam current at the microscope phosphor screen using different diameter BCAs. Here, the 1 mm aperture is the alignment hole, and “open” means a fully retracted BCA.

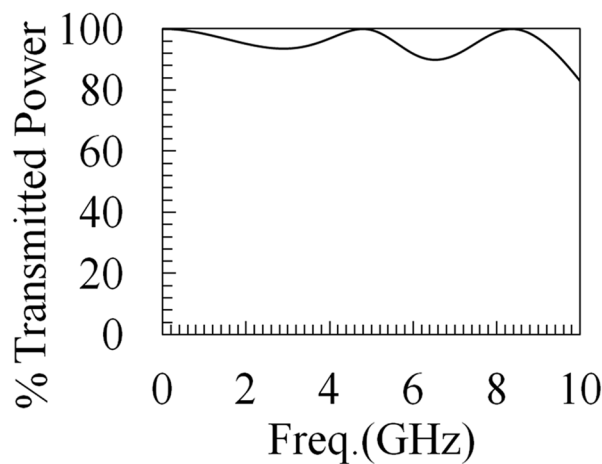


FIG. 4. Coupling efficiency for the 300 keV beam pulser, expressed as % power transmitted, for K1 and K2 as a function of the fundamental frequency,  $f_0$ .

$f_0 = 10$  GHz. Up to 6 GHz, which is the upper limit of our amplifiers, transmission is better than 90%. Efficient coupling is key to suppressing dissipative losses in the form of heat.

In addition to K1 and K2, there are three auxiliary quadrupole magnets (Q1, Q2, and Q3) within the Strobo-300 pulser assembly. The quadrupole magnets were modeled with a 3D simulation tool, Opera.<sup>20</sup> Parameters are summarized in Table I. In practice, we used vacuum compatible 20 gauge square wire with 5.2 Amp-Turn. The heat dissipation is about 6 mW, which is negligible for conduction cooling. The magnetic center was measured after fabrication.

As the CW beam enters the modulator (K1), transverse sinusoidal momentum (in the  $x - y$  plane) is added to the beam due to the electromagnetic field in K1. The transverse force on the incoming electron depends on the RF phase of K1 at the time of entry. The amplitude of the sinusoidal motion grows in a direction along the  $x - y$  plane, as the modulated beam propagates along the  $z$  direction (optic axis). After a fixed drift distance of 40 mm, the modulated electron beam enters the beam chopping aperture (BCA) at  $Z = Z_1$  in Fig. 1(b).

The aperture permits the passage of the beam each time the K1 sine function crosses zero. Since there are two zeros per cycle (when the RF phase is 0, and  $\pi$ ), the pulsed beam frequency is  $2f_0$ . In the current design, there are five discrete BCA diameters (25  $\mu\text{m}$ , 30  $\mu\text{m}$ , 35  $\mu\text{m}$ , 40  $\mu\text{m}$ , and 45  $\mu\text{m}$ ) plus a fully retracted position. Changing the BCA size is one way to determine the temporal resolution of the beam. A smaller BCA makes shorter pulses at the expense of discarding more beam. Shorter pulses (i.e., better temporal resolution) can also be achieved by increasing the power to K1, though using a smaller aperture is the preferred method because increased RF power in K1 simultaneously increases losses leading to thermal dissipation within the microscope.

In order to understand the impact of the BCA on the beam duty cycle, which is the ratio of the pulsed beam to the CW beam, we have performed multi-particle tracking simulations to study the dependency of duty cycle on various pulser parameters. The duty cycle is measured and inferred by the beam current at the CCD camera. In our pulser system, there are two tunable parameters that can impact the duty cycle: (1) RF power,  $P_{rf}$ , and (2) BCA radius  $r$ . Note, while  $f_0$  is tunable, it does not affect the duty cycle. We used Astra<sup>20</sup> to explore the effect of the two tunable parameters on the duty cycle, thus producing two sets of simulation results. In each parameter scan, all other parameters are fixed except for the one of interest. The 3D electromagnetic fields in the TWMCSSs were obtained from CST Microwave Studio<sup>20</sup> and then converted

TABLE I. Parameters of Q1, Q2, and Q3 for the Strobo-300 pulser.

Electron kinetic energy $E_k$ (keV)	300
At $ x_0  = 0.1$ mm, $B_y dz$ (Gs $\cdot$ cm)	8.13, 1.26, 0.8
Effective length $L_{eff}$ (mm)	10
Effective gradient $G_{eff} =  dB_y/dx $ (Gs/cm)	813, 126, 80
Region of uniform field gradient $r_0$ (mm)	0.1
Gradient uniformity $ G(r)/G_0 $	$<1 \times 10^{-3}$
Dimension limits (mm)	$L = W < 40, H < 15$
Working environment	In vacuum

to the Astra format. For the initial beam parameters, we used a beam with negligible size and angular divergence. The beam is uniformly distributed longitudinally in a length that is equivalent to the travel distance of 300 keV electrons in a full period at 1.0 GHz. In this case, at higher frequencies, the electrons experience at least more than one full RF cycle and the behavior can be scaled. In the simulation, we use  $N_i = 100\,000$  initial particles and examine the number of “surviving particles” at the end of the pulser  $N_f$ . The ratio (survival rate)  $\Omega = N_f/N_i$  is used as an indicator of beam current reduction, which can be conveniently compared with the experiments.

As a first-order approximation, the angular kick from K1 on the particles adjacent to the zero phase of the sinusoidal wave is linearly dependent on time ( $2\pi f_0 t$ ). Therefore, when the aperture selects only the particles that are displaced at small angles, the number of surviving particles should be linearly proportional to aperture size  $r$ . In the first simulation, we vary only  $r$  and kept  $P_{rf}$  of K1 at approximately 10 W and  $f_0$  at 3 GHz. As expected, the linear dependence of  $\Omega$  on  $r$  is shown in Fig. 5(a). The open circles are discrete simulation points, and the line is a guide to the eye.

Whereas the dependence of  $\Omega$  on  $P_{rf}$  of K1 is shown in Fig. 5(b). For this simulation,  $f_0 = 3$  GHz and the smallest BCA was assumed.

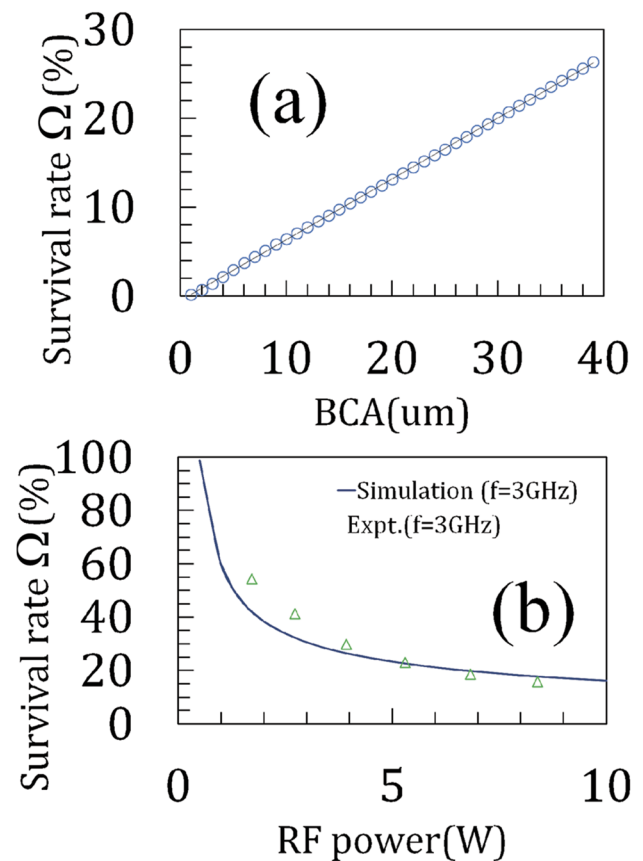


FIG. 5. Simulated dependence of  $\Omega$  on (a) the BCA radius,  $r$ , and (b) the RF power,  $P_{rf}$ , in comparison with experiments.

**TABLE II.** Results of the beam dynamic simulation for the selected cases.

Frequency $f_0$	Aperture radius ( $\mu\text{m}$ )	Simulated pulse length (ps)	Emittance $x$	Emittance $y$	Energy spread introduced (eV)
3 GHz	5	16	0.18	0.32	0.02
	10	29	0.27	0.32	0.02
	20	65	0.30	0.32	0.03
6 GHz	5	6.8	0.21	0.30	0.02
	10	13	0.28	0.30	0.03
	20	28	0.30	0.30	0.06

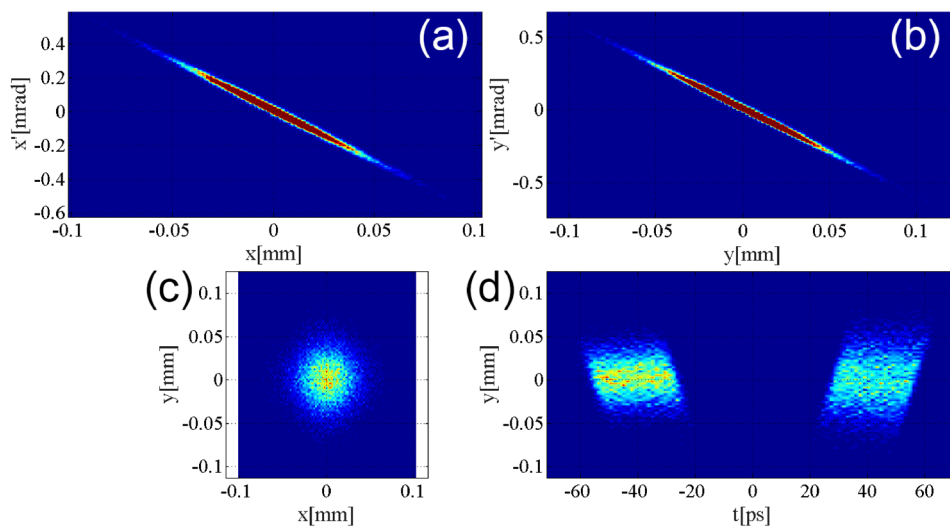
Based on theory, the survival rate is inversely proportional to the kick strength of K1, or  $\Omega \propto P_{rf}^{-0.5}$ , shown as the solid curve in Fig. 5(b). In order to validate this model, we compared the simulation with measurements obtained with the Euclid Stobo-300 pulser and the results are shown as triangles in Fig. 5(b). In the experiment,  $\Omega$  is obtained by measuring the beam current (obtained by the Faraday cup embedded in the phosphor view screen) with the pulser on and off. Because of the way that the pulsers were designed, the CW beam can be restored immediately without losing alignment when the pulser is switched off. Figure 5(b) shows that the simulation and measurement are in reasonable agreement. Disagreements may come from uncertainties in the amount of power being converted to the electromagnetic field between the TWMCS plates at run conditions, even though the RF power was calibrated at the pulser terminal.

As the pulsed beam exits the BCA, it enters the first quadrupole magnet (Q1), which was not energized for this work; usage is planned for a future modification. Exiting Q1, the beam width expands along the  $x$ - $y$  plane as it travels along  $z$ , and both the beam waist and divergence increase. Next, the pulsed beam enters the demodulator (K2). K2 is identical in construction and receives the signal with the same frequency as K1 but has independently tunable phase and amplitude. Below K2 are two more quadrupole magnets

Q2 and Q3, which are used for steering and optics matching with the original microscope components downstream.

Through the start-to-end beam dynamic simulation, we tracked the growth in emittance and energy spread as the beam traverses the pulser. Table II summarizes the simulation results of several scenarios. All simulations were conducted assuming 0.3 nm of the input beam emittance (typical of a CW beam in TEM) and 22 W of the RF input power. It shows that the emittance growths are within 10% of the original value through the pulser passage. Meanwhile, the energy spread growths are minimal. Figure 6 shows a simulated beam at exit of the pulser (this is the case presented in the last row of Table II); it shows that the emittance of the chopped beam at the pulser exit remains undisturbed under perfect compensation from K2.

In the production of a pulsed beam, and to enable pump-probe operations, signal generation and synchronization are critical. The entire pulser control system, shown in Fig. 7, contains three functional subsystems: a RF subsystem to drive K1 and K2, a DC subsystem to drive Q1-Q3, and the RF sample-pump subsystem. The system is configured using the PXIe data bus system. An ultralow-noise oscillator RF signal generator serves as both the master timing clock in the digital part of system and the master reference signal of the analog part of the system. The core controller is implemented in

**FIG. 6.** Phase space of the chopped beam at exit of the pulser: (a) transverse  $x$ -plane, (b)  $y$ -plane, (c)  $x$ - $y$  plane beam size, and (d) temporal structure.

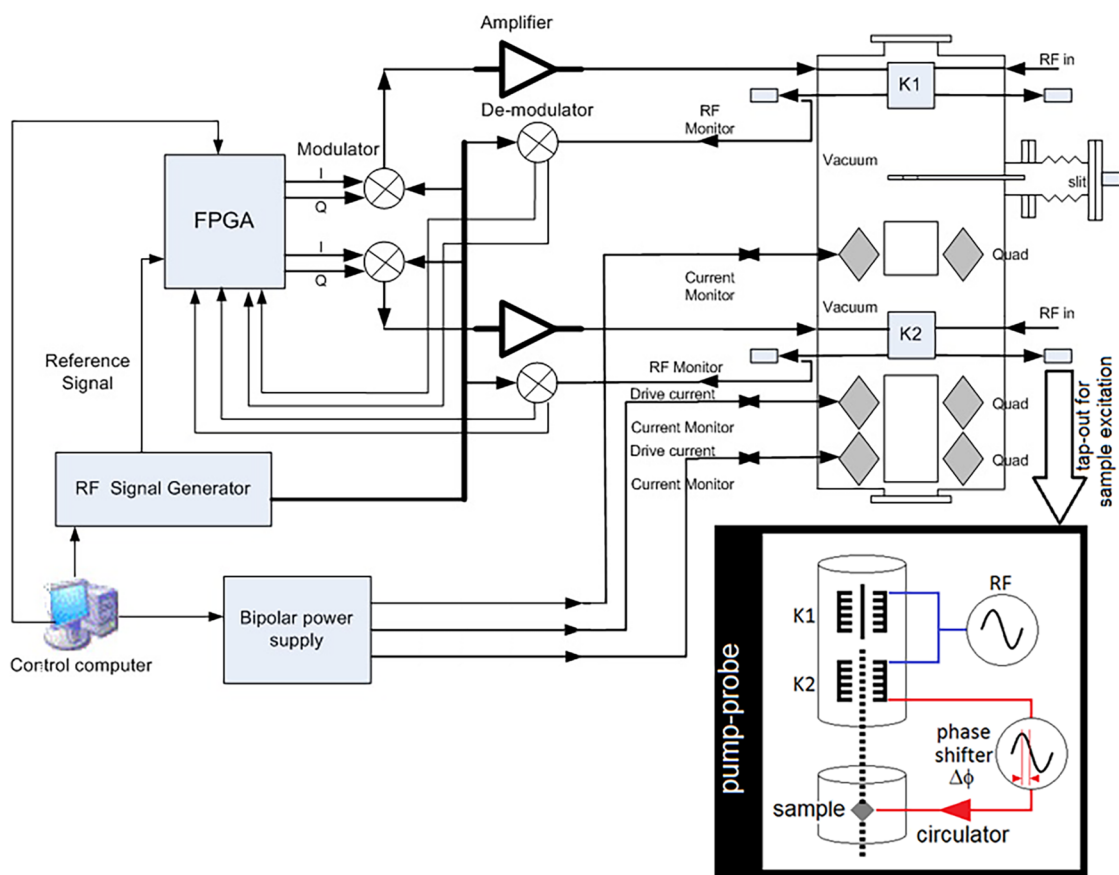


FIG. 7. Schematic of the RF control network. The inset at the bottom right-side of this figure describes a stroboscopic pump-probe setup.

the field-programmable gate array (FPGA) module to ensure rapid tuning response. The three subsystems are described in greater detail below.

### A. RF control for K1 and K2

For the uplink signal flow, a user defined frequency value  $f_0$  in the control computer is sent to the RF signal generator and the FPGA card. The FPGA card will generate two orthogonal data streams converted to two 25 MHz baseband signals (in-phase “I” and quadrature “Q”) through an interface adapter. The amplitude of the I/Q signals is defined by the user through the control computer. The I/Q signals are then conditioned and up-converted to the targeted frequency through an I/Q modulator where the carrier frequency (local oscillator) originates from the RF signal generator. After amplification by 20 W amplifiers, the up-converted RF signals are delivered to K1 and K2. For the downlink signal flow, the RF signals picked from K1 and K2 drive terminal are used for monitoring and/or forming a live feedback loop to stabilize the RF amplitude and phase. The RF pickup signals are conditioned and down-converted to the 25 MHz baseband I/Q signals through the I/Q demodulator. From here, the I/Q signals are converted back to

data streams through the same interface adapter. A proportional-integral algorithm is used for the feedback control. Feedback control is continuously provided through the FPGA card until a new  $f_0$  value is requested by the user. Aside from synchronization and delay, the feedback loop keeps timing jitter in check. Jitter is  $f_0$  dependent; the measured phase jitter at 5 GHz is  $\leq 1^\circ$  peak-to-peak, which is sub-0.5 ps rms.

### B. DC control for Q1–Q3

A 4-channel precision bipolar power supply is used to drive Q1–Q3. It can source up to 0.5 A and  $\pm 6$  V. Current resolution is 1 ppm.

### C. RF control for sample pump

The pulser control system is expandable. For pump-probe experiments, the stimulus to the sample is tapped from the RF signal leaving K1 or K2. Additional phase and amplitude control can be added to meet specific experimental needs. The inset of Fig. 7 describes one sample pump configuration, which will be further discussed in Sec. IV C.

### III. SYSTEM INTEGRATION

As shown in Fig. 1(a), both the C0 and the pulser were inserted into the TEM column, which increased the column height and weight by a total of 37 cm and  $\approx 110$  kg, respectively. Prior to the integration, the pre-partition column maintenance and alignment were conducted by the microscope vendor. All lens and deflector values in TEM and selected-area diffraction (SAD) modes were recorded. Two steps were involved for the pulser installation. The first step was the installation of the C0 and pulser outer housing, which provided structural support and the vacuum seal for the column. Completion of this step ensured a leak-free finish of the column interfaces, and the column was not expected to be taken apart again from this point forth. The second step was to insert the active pulser components into the column. Each component was individually mounted on a rectangular nonmagnetic stainless steel plate. This plate not only serves as an attachment structure but also functions as a vent port so that the pulser components may be serviced without splitting the column. While attached to the mount plate but prior to column insertion, precision optical alignment of all components was conducted with a laser on an optical table to ensure that the beam can reach the end of the pulser. With the active pulser components aligned and secured on the mount plate, the column was vented once more and the components were inserted into the pulser housing. After a long bake, the final vacuum reached  $2.5 \times 10^{-5}$  Pa prior to high-tension conditioning to 310 kV. At 300 kV operation voltage, the dark current is 111  $\mu$ A and the typical emission current is 119  $\mu$ A. With all apertures retracted and the C0 running in the fixed condition as previously described, we obtain a maximum beam current of 2.4 nA as measured by the two phosphor view screens. In order to ensure that the post-modified instrument is radiologically sound during instrument operation, 8 mm (5/16 in.) lead sheets for exterior shielding and the electrical feed-through section of the pulser and 4.76 mm (3/16 in.) lead sheets, which lined the housing interior, were used. The exposure rate was reduced to 0.05 mRem/h on contact. At the instrument operator location, the measured exposure rate was in line with background radiation levels. Upon the completion of column integration, considerable efforts were put into finding the beam and optimizing the beam condition, which included a physical translation of the C0 (perpendicular to the optic axis) via four external set-screws to find its magnetic center. It is worthwhile to point out that this is a one-time procedure when done correctly.

While the final value of gun tilt and shift were well within the range of normal operation (and not far away from the pre-partition setting), the possibility of a significant gun-shift and tilt with respect to the entrance of C0 exists.

### IV. EXPERIMENTS

We sought answers to three unknowns with this newly created instrument. The first was to verify that we still have a functional microscope post-modification, and if the images produced in the pulsed-beam and the CW modes are qualitatively similar. We answer this question by evaluating the quality of bright-field and diffraction images produced by a CW beam and comparing those to ones produced with a pulsed beam. The second was to determine the time structure of the beam. The third was to determine whether this microscope is capable of conducting pump-probe

experiments, which was the intended purpose of this modification. Unless otherwise specified, we chose  $f_0 = 2.6$  GHz for all data presented herein, noting that with the exception of intensity, the image quality is indistinguishable anywhere between 2.0 GHz and 6.0 GHz.

#### A. CW and pulsed beam comparison

In order to conduct a side-by-side comparison of the CW and pulsed-beam image quality, we assembled a collection of images generated by different modes, as shown in Fig. 8. In all cases, we used the microscope's  $\alpha = 1$  and spot size = 1 settings. The 120  $\mu$ m diameter condenser aperture was used. For the pulsed-beam images, we used the 20  $\mu$ m diameter BCA and pulsed the beam at  $f_0 = 2.6$  GHz with a pulse amplitude of 0.2 V (equivalent to 2.3 W RF power), which gave us 86 ps pulse trains. Figure 8(a) shows a bright-field TEM image of Au nanoparticles acquired at an indicated magnification of 200 kX with a CW beam and an image integration time of 1 s and Fig. 8(b) with a pulsed beam with an image integration time of 2 s. Similarly, Fig. 8(c) shows a 600 kX image recorded with a CW beam and an image integration time of 2 s and Fig. 8(d) with a pulsed beam with an image integration time of 4 s. In Fig. 8(e), we acquired a SAD pattern of the same Au sample using a CW beam at an indicated camera length of 20 cm and an image integration time of 0.25 s, and Fig. 8(f) is the same as Fig. 8(e) but with a pulsed beam and an integration time of 0.5 s. For Figs. 8(e) and 8(f), the square root of the raw intensity is displayed so that the weaker rings at higher spatial frequencies can be better highlighted. Figures 8(g) and 8(h) show the Lorentz-mode images of a patterned array of permalloy squares acquired with a CW beam (1 s integration) and a pulsed beam (2 s integration), respectively. Clearly visible in both cases are the vortex cores and the ferromagnetic domain walls. Aside from the image intensity, it is clear from this comparative series that the differences between CW and pulsed-beam images are negligible. The largest difference came from the before- and after-modification images at 600 kX (pre-modification image not shown). This microscope has an ultra-high resolution objective pole-piece (2 mm gap). At 600 kX and prior to the modification, this instrument had routinely produced lattice fringes in the images of crystalline materials. However, it is worth pointing out that we successfully acquired images with lattice fringes using the same Au sample on the modified microscope at JEOL USA headquarter.<sup>21</sup> Therefore, we assert that the loss of resolution on this instrument was not intrinsic to the modification but due to external causes that we have yet determined.

#### B. Time structure of the pulsed beam

Prior to describing how temporal resolution is measured, the different pulser operation modes are discussed. Recall that in the pulsed-beam mode [Fig. 1(c)], the phase of K2 was selected to cancel the transverse momentum of the pulsed electrons introduced by K1. Because the BCA is axially aligned with the K1 and K2 beam channels, the pulsed beam is always at the zero crossings of the RF wave driving K1 and K2. This is the origin of the beam pulse repetition rate doubling of the RF drive frequency from  $f_0$  to  $2f_0$ , and the two families of electrons (zeros and  $n\pi$ , where  $n$  is a non-zero integer) are indistinguishable as they exit the pulser.

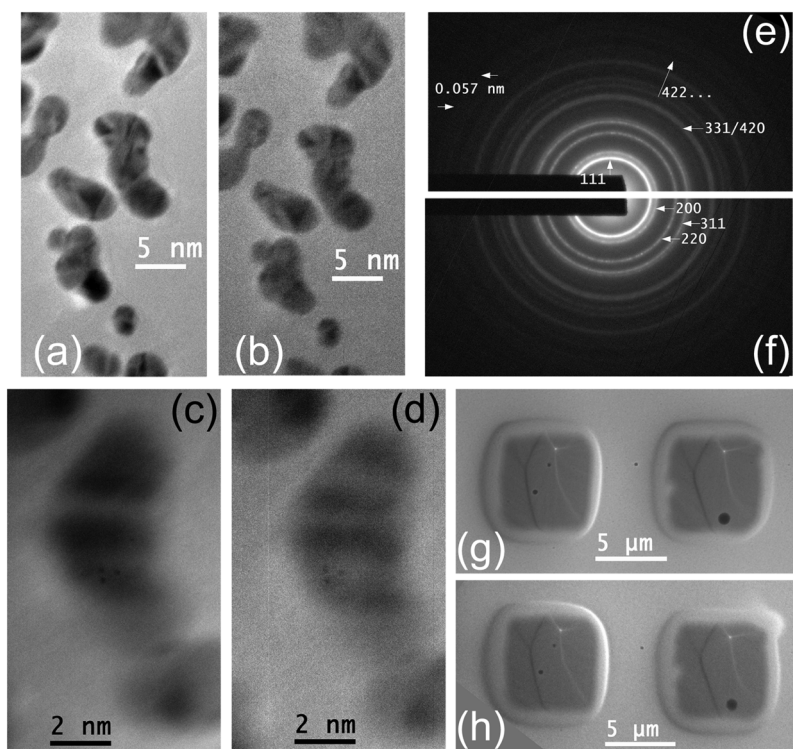


**FIG. 8.** Comparing image quality acquired with a CW and a pulsed beam (all at 2.6 GHz). A bright-field TEM image of Au nanoparticles acquired at an indicated magnification of (a) 200 kX with a CW beam, (b) 200 kX with a pulsed beam, (c) 600 kX with a CW beam, and (d) 600 kX with a pulsed beam. SAD of Au nanoparticles acquired at an indication camera length of 20 cm with (e) a CW beam and (f) a pulsed beam. A Lorentz image of permalloy squares showing magnetic contrast using (g) a CW beam and (h) a pulsed beam.

To consider the role of K2 more closely, we refer to Figs. 9(a) and 9(b). Let us now define the phase of the RF wave driving K2 ( $\phi_{K2}$ ) as relative to K1; in the pulsed beam-mode,  $\phi_{K2} = 0$ . Each electron bunch (blue ovals) exiting the BCA inherits a finite bunch duration from the diameter of the BCA. The “head” of the bunch consists of the first electrons entering the aperture; the “tail” consists of the last electrons to clear the aperture. As an electron bunch enters K2, again under the zero-crossing condition, the bunch head and tail will receive a compensational push in the  $-y$  and  $+y$  direction, respectively, for the pulsed-beam mode illustrated in Fig. 9(a). Instead, if we locked K2 out-of-phase with respect to K1 (i.e.,  $\phi_{K2} = \pi$ ), we operate in the streaked-beam mode. In this case, K2 acts not to cancel the transverse momentum in the electron bunch leaving the BCA but increases it. The bunch head and tail entering K2 will receive an added pull in the  $+y$  and  $-y$  directions, respectively, in the streaked-beam mode illustrated in Fig. 9(b). As the bunch exits K2 and down-drifts in  $z$ , the temporal information in the bunch is encoded along the  $y$  direction. The recorded beam width in the  $y$ -direction is, therefore, a good proxy for the pulse length of the beam.

The pulse length (in units of seconds) is related to the beam’s bunch length,  $\sigma_z$  (with units in meters), through the speed of the electron. The following equation<sup>23</sup> expresses  $\sigma_z$  in terms of known and measurable quantities:

$$\sigma_z = \frac{E_k}{keV_k D} \sqrt{\sigma_y^2 - \sigma_{y0}^2}. \quad (2)$$

Here,  $E_k$  is the kinetic energy of the beam,  $k$  is the wavenumber of the input RF wave,  $e$  is the electron charge,  $V_k$  is the modulation strength of K2,  $D$  is the drift distance, and  $\sigma_y$  and  $\sigma_{y0}$  are the beam widths on the screen with K2 on and off, respectively. It is worth pointing out that in the streaked-beam mode, Eq. (2) does not account for the effect of non-uniform modulation in K2 due to the finite beam size (e.g., if the beam waist is comparable to the stripline gap of K2), resulting from transverse momentum induced by K1.

In Fig. 9(c), the tunability of the pulse length is demonstrated by varying the RF power delivered to K1 in the streaked-beam mode. We should point out that even though all apertures, downstream of the pulser, were retracted, the down-column optical conditions are opaque to us, other than the fact that we seemed to have observed an un-obstructed beam on the CCD camera. To ensure that our results are within reasonable bounds and not obscured by possible beam clipping, we conducted a simulation using ideal streaking parameters for each experimental K1 RF power. We then normalize a selected measurement point to one simulation case (e.g., assume that the bunch length in simulation and experiment agrees with each other at 6 W of K1 input) and scaled all other measurements to the same normalization factor. For comparison, both the simulation and measurements are shown in Fig. 9(c). Although the simulation and the measurements do not agree perfectly, an overarching trend can be seen: higher RF power to K1 decreases bunch length and improves temporal resolution. Figures 9(d) and 9(e) show the images of the streaked-beam with K1 operating at 6 W and 8.8 W, respectively.

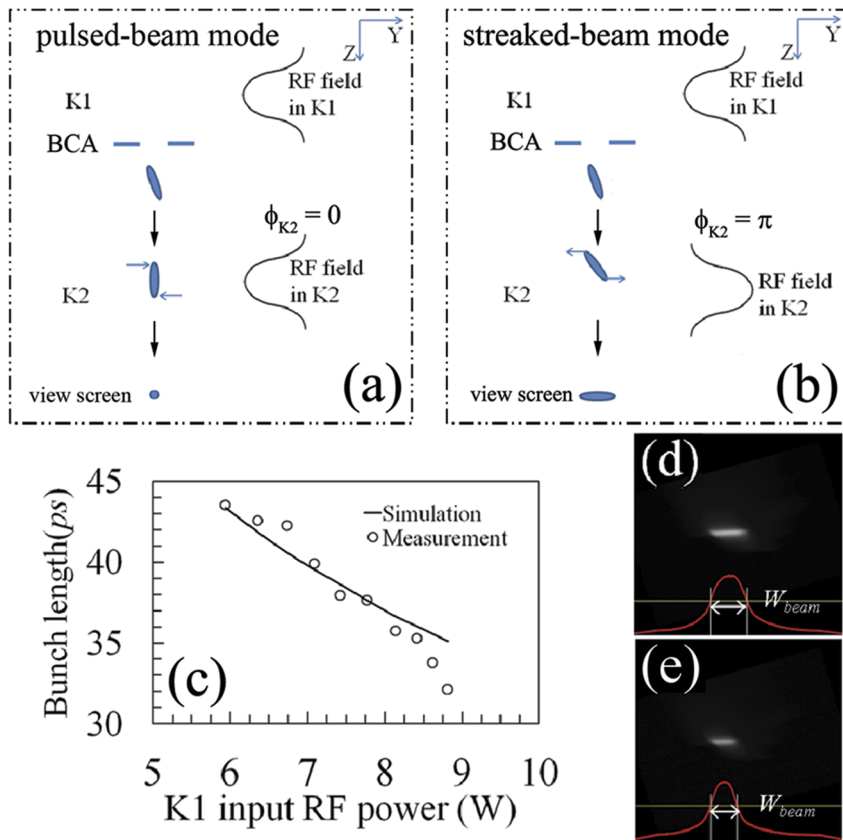


**FIG. 9.** (a) Schematic of transverse momentum cancellation in the pulsed-beam mode. (b) Schematic of transverse momentum broadening in the streaked-beam mode. The pulse length (temporal resolution) of the beam is encoded along the beam-stretch direction. (c) Comparison of the measured and simulated bunch length. (d) and (e) show the beam widths recorded in the streak-beam mode by using a CCD camera with K1 RF power at 6 W and 8.8 W, respectively. Note that higher RF power produces shorter bunch lengths and hence better temporal resolution. The RF frequency was 3 GHz in this measurement.

Increasing K1 power produces shorter beam pulses, as seen in the full-width at half-maximum pulse length [labeled  $W_{beam}$  in Figs. 9(d) and 9(e)]. The pulse lengths observed here are between 30 ps and 45 ps, which is longer than the values previously measured using the 200 keV microscope.<sup>21</sup> This is due to the increased stiffness of the 300 keV beam in comparison with the 200 keV beam. The power requirement to produce the same oscillation is doubled for the 300 keV beam with respect to the 200 keV beam (the required RF power  $P_{rf} \propto \beta^4 E^2$ , where  $\beta$  is the relativistic velocity of the particle divided by the speed of light and  $E$  is the total energy of the particle).

### C. A stroboscopic pump-probe experiment

To demonstrate that this instrument can be deployed for stroboscopic pump-probe experiments, we fabricated a device consisting of two interdigitated combs, which may be treated as a series of parallel plate capacitors (Fig. 10). The combs were fabricated using a silicon on insulator (SOI) wafer and a typical SOI microfabrication process. The total length of each comb is 1.25 mm; each tine is 75  $\mu\text{m}$  long and 7  $\mu\text{m}$  wide. The tine pitch on both combs is 20  $\mu\text{m}$ , which makes a  $g = 3 \mu\text{m}$  gap between interleaved tines. The tines are etched  $L = 25 \mu\text{m}$  deep along the beam-path dimension. The resistivity of the silicon device layer is 0.01  $\Omega \text{ cm}$ , with a capacitance of  $\sim 0.5 \text{ pF}$ . We estimated a relative permittivity of  $\sim 12$ . Using the

following equation for charged parallel plates,<sup>24</sup> where  $e$  is the electron charge and  $E/E_0$  is the ratio between the beam energy and the electron rest energy, we can achieve  $\theta = 1 \text{ mrad}$  deflection on 300 keV electrons with plate potential,  $u = 60 \text{ V}$ :

$$\theta = \frac{euL}{2gE} \frac{1 + \frac{E}{E_0}}{1 + \frac{E}{2E_0}}. \quad (3)$$

With an RF input, the wavelength in a dielectric medium is given by Eq. (4). For a 2.6 GHz wave, the wavelength in vacuum is 11.5 cm, but only about 3 cm in our comb. For perspective, our 1.25 mm comb spans less than 5% of a full wave at 2.6 GHz,

$$\lambda = \frac{c}{v\sqrt{\epsilon_r}}. \quad (4)$$

The inset at the bottom right of Fig. 7 is a simplified schematic illustrating the key relationship between the probe beam and the sample excitation. As the RF signal makes its way through K1 and K2, we tapped off the traveling wave at the exit end of K2. Untapped exit waves are 50  $\Omega$  terminated to eliminate reflections. The total length of conductors (red line) connecting the K2 tap-out port and the sample is the absolute path difference between the drive signal and the pump signal and is the origin of the phase difference ( $\phi$ ) between the pump and the probe. This absolute phase difference is difficult to measure accurately; however, an analog phase

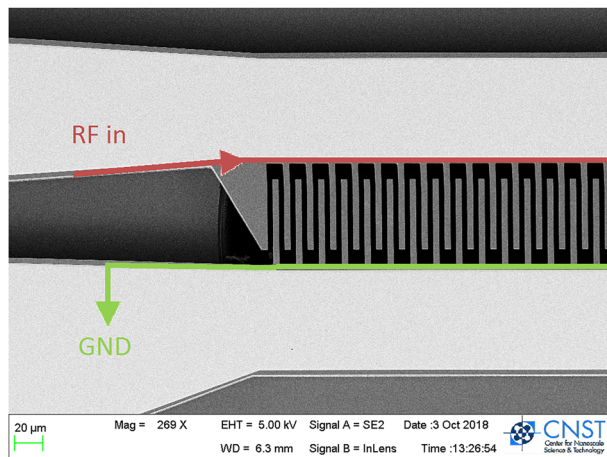


**FIG. 10.** SEM image showing a pair of interdigitated combs. Only one comb receives an electrical signal; the other comb is always grounded.

shifter inserted into the signal path can add an arbitrary phase  $\Delta\phi$  to the signal reaching the sample. The total phase difference between pump and probe is, therefore,  $(\phi + \Delta\phi)$ . Because  $\Delta\phi$  can be anything, the phase shifter can, in effect, recover all phases within a cyclical event. The phase shifter has a precision mechanical hand-crank that changes  $\Delta\phi$  in units of degrees per gigacycle ( $^\circ/\text{Gc}$ ). Following the phase shifter, a circulator is inserted just before the signal enters the sample holder. The purpose of a circulator is to permit the unidirectional transmission of power; it is an insurance against potential reflected power that could damage costly or irreplaceable hardware. Finally, the signal travels to a commercially available biasing sample holder with coaxial feed-throughs and arrives at the sample in the following sequence: coaxial cables terminated by non-standard push-pull connectors, 27 cm of coaxial cables followed by 2 cm of bare wires connecting up to a spring-loaded connector clip, a 1.7 cm printed circuit board, and finally  $\sim 0.5$  cm of Au wire bonds. Each of the previously described junctions is a source of impedance mismatch. Additionally, the section of bare wires is likely to be a significant contributor to crosstalk. The result is high losses in the GHz range due to the holder alone, as measured by using a network analyzer. At 2.6 GHz, the insertion loss is close to  $-20$  dB due to the sample holder; at other frequencies (e.g., 4.2 GHz and 5.6 GHz) losses approach  $-50$  dB. Details of the sample holder measurement will appear in a separate publication. For this experiment, we selected two passable frequencies,  $f_0 = 2.6$  GHz and 3.5 GHz, to verify that we can measure pump-probe effects. We remind the reader once more that the strobe frequency is twice the sample excitation frequency in this setup.

For the set of experiments described here, we energized only one comb (the active comb), while the other was held at ground potential (the ground comb). To verify that the device was working prior to launching the pump-probe experiment, we applied a 40 V DC and a 40 V AC 60 Hz bias on the active comb. A 40 V DC bias to the active comb translated to a net deflection in the path of the 300 keV electrons toward the active tines. When energized, we expect the active tines to appear narrower. This was in fact observed as shown in Fig. 11(a). On the other hand, 40 V AC applied to

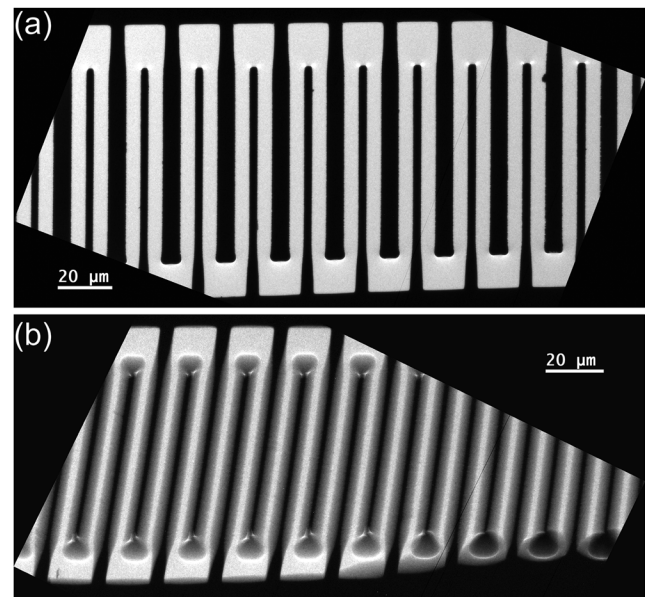


**FIG. 11.** Image of the combs with (a) 40 V DC bias and (b) 40 V AC 60 Hz bias. We note here that the warping of the image seen in (b) is not intrinsic to the AC signal, as this was observed in the DC case as well. Rather, the warping increased with the duration of the experiment, suggesting a charging effect.

the active comb meant that its potential difference relative to the ground comb varies smoothly between  $\pm 40$  V every  $1/60$ th of a second. The time-averaged blur of this alternating deflection is evident in Fig. 11(b), which is a 1 s recording. This set of images indicates that the comb is functioning as expected.

Next, we performed stroboscopic imaging on the comb with a 5.2 GHz electron pulse train and a 2.6 GHz sinusoidal sample excitation. The setup for the RF stroboscopic pump-probe measurements is nearly identical to the DC and the 60 Hz case, except that the combs were synchronously pumped at one end and 50  $\Omega$  terminated at the other end. Figure 12(a) shows three tines (two active tines and one ground tine in between them) under different phase shift conditions from  $\Delta\phi = 0^\circ$  to  $182^\circ$  in increments of  $10^\circ$  on the phase shifter readout, which is equal to  $\Delta\phi = 2.6 \text{ Gc} \times 10^\circ/\text{Gc} = 26^\circ$ . Note that this image series was obtained from the 200 keV sister microscope, which has a similar pulser (Euclid Strobo 200) installed. While we also collected many stroboscopic pump-probe images with the 300 keV instrument, these are not shown because the tines collectively exhibited a somewhat different periodic blur pattern; experimental findings and a discussion of those experiments are available in the [supplementary material](#). Conditions that led to the differences in tine blurring patterns between the two microscopes are under investigation. However, we believe that the data obtained from the 200 keV microscope offer a more straightforward explanation of the physics inside the comb during excitation.

In Fig. 12(a), when  $\Delta\phi$  is close to zero, the edges of each tine (dark) appeared sharp. Increasing  $\Delta\phi$  causes blur at the boundaries between the tines and the gaps (bright), and this is due to the electrostatic deflection of the imaging electrons. The blur width,

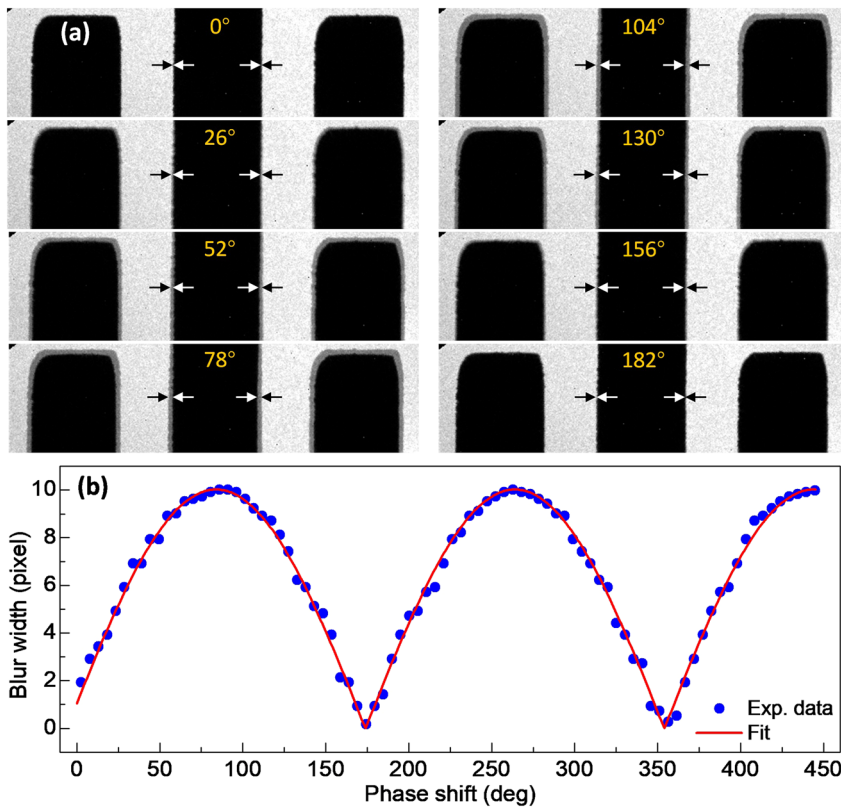


**FIG. 12.** Stroboscopic pump-probe imaging experimental results. (a) Stroboscopic pump-probe image series of a comb tine with  $f_0 = 2.6$  GHz at various values of phase shift,  $\Delta\phi$ . Small black and white arrows indicate the blur width. (b) The blur width ( $W$ ) variation as a function of  $\Delta\phi$ . The blue dots are experimental data, and the red curve is the fitted result.

$W$ , reaches a maximum at about  $91^\circ$ , then decreases again with further increases to  $\Delta\phi$  until it vanishes at  $\approx 182^\circ$ . The cycle is repeated again starting at  $\approx 182^\circ$ . While it is instructive to compare the 60 Hz and the 2.6 GHz images side-by-side, it is important to remember that the 60 Hz images are time-averaged and the GHz images are stroboscopic, even though the blur pattern through the comb appears similar (i.e., blur on all boundaries between tines and gaps). In the 60 Hz image, the time-averaged intensity of the blur at the boundary has a graded spatial profile varying between the gap and the tine. This is consistent with the continuous blurring of a 60 Hz sine wave. In the stroboscopic pump-probe image, the intensity profile of the blur is a step function, where the intensity is exactly midway between the gap and tine level. Note that the blur widths also appear much smaller in the GHz stroboscopic images due to the poor coupling efficiency of the holder in the GHz range.

To further analyze the effect that changing  $\Delta\phi$  has on  $W$ , we focused on one tine and repeated the measurement in increments of  $1^\circ$  on the phase shifter (equal to increments of  $\Delta\phi = 2.6^\circ$ ) and presented the results in Fig. 12(b). We used a simple sine function [Eq. (5)] to describe  $W$  of a given tine as a function of  $\Delta\phi$ . The blue dots are experimental data, and the red curve is the fitted result. Equation (5) has three free-fitting parameters:  $A$  is the amplitude of blur,  $f_0$  is the frequency of the fundamental phenomenon that underlies the periodicity seen in the blur, and  $\phi$  is the phase shift inherent to the physical path length from cabling and conduction

pathway (and should be invariant for a given experimental setup),

$$W = A|\sin(f_0(\phi + \Delta\phi))|. \quad (5)$$

Here, the quantity of keen interest is the fitted results for  $f_0$ ; if we were in fact conducting a stroboscopic pump-probe experiment, then the fitted value of  $f_0$  should match the  $f_0$  supplied to the control PC. This was in fact what we saw for stroboscopic pump-probe images obtained from both microscopes. Another parameter of potential interest from the fit is  $\phi$ , as it informs us of an absolute phase reference for a particular experimental setup. We expected  $\phi$  to be different for different frequencies (wavelengths are different), for the two combs (total path lengths, including the lengths of the wire bonds are different), and for the two microscopes (different cables were used). We showed in this experiment that we were sensitive to the absolute phase and phase difference in our setup, and these are measurable quantities for future experiments where this information may be important. However, since the absolute phase difference between the pulse and the pump (given by  $\phi + \Delta\phi$ ) can be arbitrarily chosen by the mechanical phase-shifter or referencing a different point along the path, we simplified the following discussion on the image contrast mechanism to  $\Delta\phi$  with the understanding that a zero-phase difference reference point was chosen.

To help us understand the observed periodic blur pattern as a function of  $\Delta\phi$ , we consider Fig. 13, which is a timing schematic showing the relationship between the pump RF signal and the probe

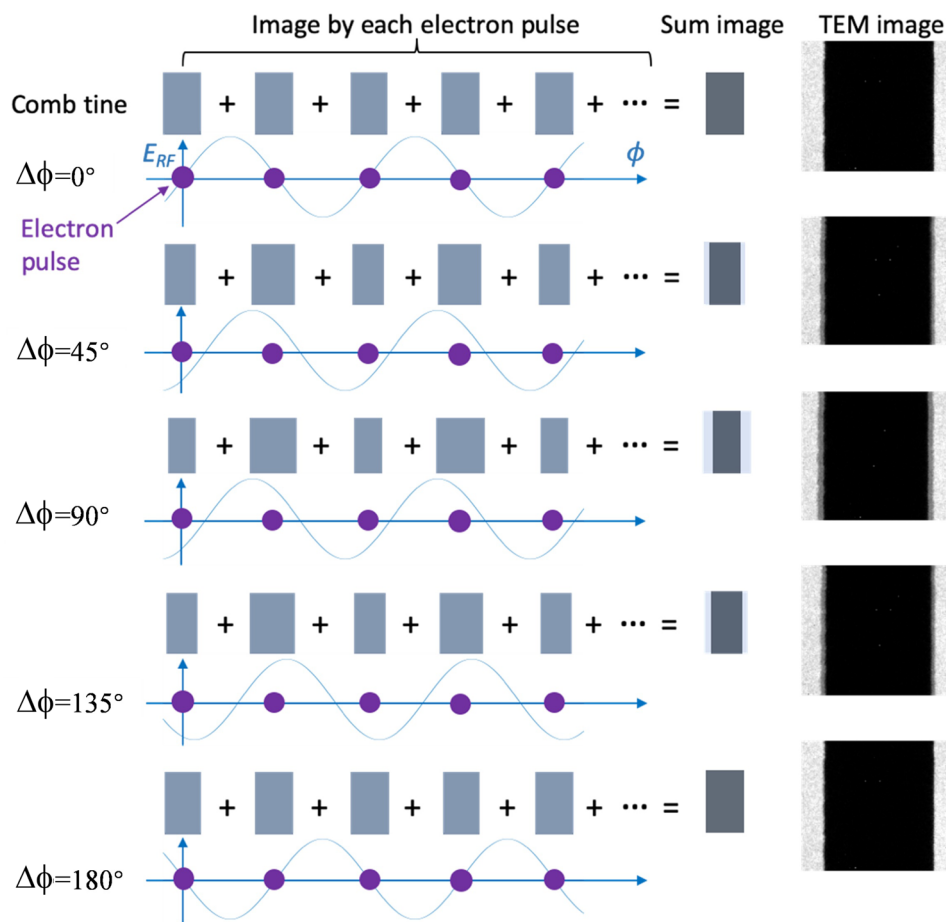


**FIG. 13.** Origin of the blur pattern formation in the stroboscopic pump-probe experiment of the comb sample under 2.6 GHz RF excitation and a 5.2 GHz pulsed beam at different phase shifts. The right-most column shows the corresponding experimental images.

beam. This schematic illustrates the one tine on the active comb, which when  $\Delta\phi$  is set to zero, there is no phase difference between the probe electron pulse and the pump RF signal. For a comparison, the experimental images are shown in the same figure along the right column. On this tine, at  $\Delta\phi = 0^\circ$ , the electric potential of the active tine with respect to the ground comb is zero; thus, no deflection is applied for each of the imaging electron pulses. In the stroboscopic mode, each electron pulse probes the sample under the same state during the cycles of stimulus. Because the final readout image is the sum of all the images undergoing the same portion of a cyclical process, the features should appear very sharp, as shown in the top image. At  $\Delta\phi = 45^\circ$ , for each pair of probe pulses arriving at the tine, electric potentials of the active tine with respect to the ground comb have the same magnitude, but opposite signs. Therefore, the pulse pair is deflected in opposite directions in the gap, which results in a narrower tine image formed by one electron pulse in the pair and a wider tine image formed by the other. As a result, the final readout image showed a blur pattern on both sides of the active tine (see the image accompanying  $\Delta\phi = 45^\circ$  in Fig. 13). Continuing the previous trend, when  $\Delta\phi = 90^\circ$ , electric potentials of the active tine with respect to the ground comb again have the same magnitude and opposite signs. However, the deflection

amplitude here is at a maximum, resulting in maximum blur observed with the corresponding image (third panel in Fig. 13). The phase  $\Delta\phi = 135^\circ$  is qualitatively identical to  $\Delta\phi = 45^\circ$ . The only difference is that the sign of electric potentials of the active tine with respect to the ground comb is exchanged at the arrival time of a pulsed electron pair. Under this condition, the readout image is identical to  $\Delta\phi = 45^\circ$  (see that the images accompanying  $\Delta\phi = 45^\circ$  and  $\Delta\phi = 135^\circ$  are the same in Fig. 13). At  $\Delta\phi = 180^\circ$ , the active and ground combs are again equipotential, which is accompanied by an image with sharp edges, which is similar to the  $\Delta\phi = 0^\circ$  case. With a further increase in  $\Delta\phi$  from  $180^\circ$  to  $360^\circ$ , the cycle of blur-to-sharp patterns repeats itself, resulting in the periodic change of the blur width.

## V. SUMMARY, OUTLOOK, AND CONCLUSION

To summarize, we have retrofitted an in-service 300 keV thermionic emission TEM so that it can perform time-resolved stroboscopic experiments. Through GHz sinusoidal excitation of an interdigitated MEMS comb sample, we proved that instruments of this type are capable of performing in the GHz stroboscopic pump-probe regime. Materials amenable to this method of query have to

be periodic and repeatable. Candidate systems include ferromagnets, memristors, MEMS and NEMS (nanoelectromechanical systems), and batteries. Unlike other time-resolved TEMs, this one requires no laser and our pulsed-beam is, in principle, broadband tunable between 40 MHz and 12 GHz. We achieved a temporal resolution of 30 ps at 18% beam duty cycle; this is an impressively high yield compared to the stroboscopic mode performed with a photoemission TEM where the laser repetition rates are generally in MHz.

Because the probe frequency is twice the pump frequency, a clean pump-probe experiment should ideally be accomplished by doubling the pump frequency prior to sending it into the sample. Frequency doublers with small insertion losses are commercially available and, where possible, will be used in future experiments. The key point to consider about doubling the pump frequency is that this new frequency should reside within a pass-band of the sample holder. Ideally, one could design a sample holder with good signal transfer characteristics across a wide frequency range.

Assuming that the signal attenuation problem can be resolved with the holder, we have near limitless configurability in the way that the pump (sample) is addressed because the pump and the probe are both centrally synchronized electrical signals. In this work, we demonstrated the simplest case, where we drove the sample with the same sinusoidal wave exiting the pulser. However, one can easily insert a pulse shape generator before the sample, should the sample require a sharp rise-trigger. With the same electrical signal, one can translate the input into an on-sample magnetic signal by standard nanofab patterning techniques. By the same principle, on-chip oscillators, antennas, inductors, heat, and light sources can be fabricated for sample excitation. Should an experiment require precise timing, an external standard such as a Rb clock can be used instead of the on-board reference.

Two research groups have recently demonstrated that certain electron-beam sensitive samples can, nonetheless, be successfully examined if the dose rates are kept below certain thresholds.<sup>25,26</sup> Inspired by these results, we have begun a feasibility study on using the pulser as a beam-management device. If proven, this device could have consequences for the biological EM community. Beyond this, the next logical effort would be to determine whether this technology can enable stroboscopic scanning TEM and the associated spectroscopic methods.

It was evident to many researchers that the future of numerous technologies hinges on our ability to decode dynamic processes occurring at the smallest length scales. This project began with a simple premise that time-resolved electron microscopy should be broadly available and accessible. As the cost of new instruments may be prohibitive to many research groups, it mattered to us that this modest technology can be deployed to extend the useful life of in-service microscopes and detectors. While writing this manuscript, this team succeeded in a third retrofit, a 200 keV sister instrument at Brookhaven National Laboratory, and it has begun producing results, some of which appeared in this work. Because of the combination of high repeat-rates and beam duty-cycle, we can acquire time-resolved images without upgrading our CCD cameras. These recent success stories convinced us that this technology can make time- and frequency-domain physics broadly accessible for the materials community.

## SUPPLEMENTARY MATERIAL

The [supplementary material](#) contains the data and a brief discussion of the data from stroboscopic pump-probe experiments using the 300 keV microscope.

## ACKNOWLEDGMENTS

This collaboration is grateful for the crucial advice and assistance from JEOL USA: Hideaki Arima, Bob Pohorenc, John Guerin, Joseph Girgis, Mike McKie, Scott Johnson, Bob Connor, Barbara Lear, Don Tylutki, Rick Poncheri, and Mark Komin. We are also grateful for the consultation from IDES and, in particular, to Bryan Reed for his interdigitated comb benchmarking suggestion. This work was supported by the DOE BES SBIR program (Grant No. DE-SC0013121). The research at BNL was supported by the U.S. Department of Energy, Office of Basic Energy Sciences, Division of Materials Science and engineering, under Contract No. DE-SC0012704. An NIST microscope was commissioned under Award No. SB1341-16-CN-0035.

## REFERENCES

- 1 A.-C. Milazzo, P. Leblanc, F. Duttweiler, L. Jin, J. C. Bouwer, S. Peltier, M. Ellisman, F. Bieser, H. S. Matis, H. Wieman, P. Denes, S. Kleinfelder, and N.-H. Xuong, *Ultramicroscopy* **104**, 152 (2005).
- 2 L. Jin, A.-C. Milazzo, S. Kleinfelder, S. Li, P. Leblanc, F. Duttweiler, J. C. Bouwer, S. T. Peltier, M. H. Ellisman, and N.-H. Xuong, *J. Struct. Biol.* **161**, 352 (2008).
- 3 G. McMullan, S. Chen, R. Henderson, and A. R. Faruqi, *Ultramicroscopy* **109**, 1126 (2009).
- 4 G. McMullan, A. T. Clark, R. Turchetta, and A. R. Faruqi, *Ultramicroscopy* **109**, 1411 (2009).
- 5 V. A. Lobastov, R. Srinivasan, and A. H. Zewail, "Four-dimensional ultrafast electron microscopy," *Proc. Natl. Acad. Sci. U. S. A.* **102**(20), 7069 (2005).
- 6 A. H. Zewail, *Annu. Rev. Phys. Chem.* **57**, 65 (2006).
- 7 T. LaGrange, M. R. Armstrong, K. Boyden, C. G. Brown, G. H. Campbell, J. D. Colvin, W. J. DeHope, A. M. Frank, D. J. Gibson, F. V. Hartemann, J. S. Kim, W. E. King, B. J. Pyke, B. W. Reed, M. D. Shirk, R. M. Shuttlesworth, B. C. Stuart, B. R. Torralva, and N. D. Browning, *Appl. Phys. Lett.* **89**, 044105 (2006).
- 8 D. J. Flannigan and A. H. Zewail, *Acc. Chem. Res.* **45**, 1828 (2012).
- 9 A. Feist, N. Bach, N. Rubiano da Silva, T. Danz, M. Möller, K. E. Priebe, T. Domröse, J. G. Gatzmann, S. Rost, J. Schauss, S. Strauch, R. Bormann, M. Sivis, S. Schäfer, and C. Ropers, *Ultramicroscopy* **176**, 63 (2017), 70th Birthday of Robert Sinclair and 65th Birthday of Nestor J. Zaluzec PICO 2017 – Fourth Conference on Frontiers of Aberration Corrected Electron Microscopy.
- 10 T. LaGrange, B. W. Reed, and D. J. Masiel, *MRS Bull.* **40**, 22 (2015).
- 11 P. Binev, W. Dahmen, R. DeVore, P. Lamby, D. Savu, and R. Sharpley, in *Modeling Nanoscale Imaging in Electron Microscopy*, Nanostructure Science and Technology, edited by T. Vogt, W. Dahmen, and P. Binev (Springer US, Boston, MA, 2012), pp. 73–126.
- 12 A. Stevens, L. Kovarik, P. Abellan, X. Yuan, L. Carin, and N. D. Browning, *Adv. Struct. Chem. Imaging* **1**, 10 (2015).
- 13 X. Liu, S. Zhang, A. Yurtsever, and J. Liang, *Micron* **117**, 47 (2019).
- 14 D. A. Plemmons and D. J. Flannigan, *Chem. Phys. Lett.* **683**, 186 (2017), Ahmed Zewail (1946–2016): Commemoration Issue of Chemical Physics Letters.
- 15 G. S. Plows and W. C. Nixon, *J. Phys. E: Sci. Instrum.* **1**, 595 (1968).
- 16 K. Soma, S. Konings, R. Aso, N. Kamiuchi, G. Kobayashi, H. Yoshida, and S. Takeda, *Ultramicroscopy* **181**, 27 (2017).
- 17 A. Lassise, P. H. A. Mutsaers, and O. J. Luiten, *Rev. Sci. Instrum.* **83**, 043705 (2012).

- <sup>18</sup>J. Qiu, G. Ha, C. Jing, S. V. Baryshev, B. W. Reed, J. W. Lau, and Y. Zhu, *Ultramicroscopy* **161**, 130 (2016).
- <sup>19</sup>W. Verhoeven, J. F. M. van Rens, E. R. Kieft, P. H. A. Mutsaers, and O. J. Luiten, *Ultramicroscopy* **188**, 85 (2018).
- <sup>20</sup>Certain commercial equipment, instruments, or materials are identified in this presentation to specify the experimental procedure adequately. Such identification is not intended to imply recommendation or endorsement by the National Institute of Standards and Technology, nor is it intended to imply that the materials or equipment identified are necessarily the best available for the purpose.
- <sup>21</sup>C. Jing, Y. Zhu, A. Liu, K. Schliep, X. Fu, Y. Zhao, E. Montgomery, W. Rush, A. Kanareykin, M. Katz, and J. Lau, *Ultramicroscopy* **207**, 112829 (2019).
- <sup>22</sup>K. Zhang and D. Li, *Electromagnetic Theory for Microwaves and Optoelectronics*, 2nd ed. (Springer, Berlin; New York, 2008), Chap. 7.
- <sup>23</sup>J. Shi, H. Chen, C. Tang, Y. Du, W. Huang, L. Yan, R. Li, and Q. Du, Proc. Part. Accel. Conf. **TH5PFP094**, 3429–3432 (2009).
- <sup>24</sup>L. Reimer, *Transmission Electron Microscopy: Physics of Image Formation and Microanalysis*, Springer Series in Optical Sciences, 3rd ed. (Springer-Verlag, Berlin Heidelberg, 1993).
- <sup>25</sup>E. J. VandenBussche and D. J. Flannigan, *Nano Lett.* **19**(9), 6687 (2019).
- <sup>26</sup>C. Kisielowski, P. Specht, B. Freitag, E. R. Kieft, W. Verhoeven, J. F. M. van Rens, P. Mutsaers, J. Luiten, S. Rozeveld, J. Kang, A. J. McKenna, P. Nickias, and D. F. Yancey, *Adv. Funct. Mater.* **29**, 1807818 (2019).